Satellite decay in flattened dark matter haloes

Jorge Peñarrubia[1], Pavel Kroupa[2] & Christian M. Boily[1,3]

[1] *Astronomisches Rechen-Institut, Mönchhofstrasse 12-14, 69120 Heidelberg, Germany*
[2] *Institut für Theoretische Physik und Astrophysik, Universität Kiel, SD-24098 Kiel, Germany*
[3] *Observatoire Astronomique, 11 rue de l'Université, F-67000 Strasbourg, France*

1 February 2008

ABSTRACT

We carry out a set of self-consistent N-body calculations to compare the decay rates of satellite dwarf galaxies orbiting a disc galaxy embedded in a dark matter halo (DMH). We consider both spherical and oblate axisymmetric DMHs of aspect ratio $q_h = 0.6$. The satellites are given different initial orbital inclinations, orbital periods and mass. The live flattened DMHs with embedded discs and bulges are set-up using a new fast algorithm, MaGalie (Boily, Kroupa & Peñarrubia 2001).

We find that the range of survival times of satellites within a flattened DMH becomes $\sim 100\%$ larger than the same satellites within a spherical DMH. In the oblate DMH, satellites on polar orbits have the longest survival time, whereas satellites on coplanar prograde orbits are destroyed most rapidly. The orbital plane of a satellite tilts as a result of anisotropic dynamical friction, causing the satellite's orbit to align with the plane of symmetry of the DMH. Polar orbits are not subjected to alignment. Therefore the decay of a satellites in an axisymmetric DMH may provide a natural explanation for the observed lack of satellites within $0 - 30°$ of their host galaxy's disc (Holmberg 1969; Zaritsky & González 1999).

The computations furthermore indicate that the evolution of the orbital eccentricity e is highly dependent of its initial value $e(t = 0)$ and the DMH's shape. We also discuss some implications of flattened DMHs for satellite debris streams.

Key words: stellar dynamics – methods: numerical – galaxies: evolution – galaxies: kinematics and dynamics – galaxies: spiral – dwarf satellites

1 INTRODUCTION

Non-spherical mass distributions around galaxies and galaxy clusters are needed to reconcile the dynamics with lensing statistics (Maller et al. 2000; González et al. 1999; Maller et al. 1997; Keeton & Kochanek 1998) or galactic disc warps (Binney 1992). In CDM cosmogony, aspherical bound dark matter haloes ($\equiv$ DMHs) form as a result of gravitational clustering. Dubinsky (1994) finds in his computer simulations a Gaussian distribution of DMH aspect ratios, $q_h \equiv c/a > 0$, where c and a are the minor and major axes of an oblate spheroid, of mean $< q_h >= 1/2$ and dispersion equal to 0.15. In a CDM framework, therefore, DMHs may achieve an aspect ratio as high as $q_h = 0.65$, covering a range of values more than adequate to account for lensing data: for instance, Maller et al. (2000) find that for the galaxy B1600 + 434, $0.5 < q_h < 0.75$. The inferred morphology of the DMH, however, depends on the details of its radial mass profile and embedded baryonic galaxy components, such as the disc and bulge of a spiral galaxy, and is, on the whole, a loosely constrained quantity. For instance, Olling & Merrifield (2000) studying the axis-ratio of the Milky Way by

two independent methods (first, by the measurements of its rotational curve and the amount of dark matter in the solar neighborhood and, second, by the variation in thickness of HI emission) find a consistent value of $q_h \sim 0.8$, although it depends strongly on the measurement of the Milky Way's parameters.

In general, different techniques yield a wide range of values for q_h. Models of decaying neutrinos (Sciama 1990) or cold molecular gas (Pfenniger et al. 1994) suggest a minimum value $q_h = 0.2$, whereas models of the Milky Way halo suggest $q_h = 0.9$ to account for the narrow debris stream of the Sagittarius dwarf (Ibata et al. 2001). The measure of axis-ratios throughout a DMH is riddled with uncertainties due to the unknown profile of the halo. Furthermore, lensing or stellar kinematics yield diagnostics that are constrained in the inner region mainly, where density gradients are the largest. The Sagittarius dwarf data suggest that the inner region of the MW DMH would be spherical, yet questions arise as to whether the same hold true on scales approaching 100 kpc or more.

The dynamics of galactic satellites may help constrain DMH profiles on large scales by direct observations of their

distribution around the host galaxy. Holmberg (1969) and Zaritsky & González (1999) point out that satellites around disc galaxies are found more often aligned with the poles of the host galaxy, the so-called 'Holmberg effect'. One possible reason for this effect is the enhanced satellite-disc coupling for co-planar satellite orbits. Quinn & Goodmann (1986), however, find in their N-body study that discs alone cannot account for the original statistical distribution of Holmberg's data.

A remedy may be sought in the form of an extended non-spherical DMH. An anisotropic velocity (and mass) distribution will cause a satellite's orbit to align with the axes of the velocity ellipsoid of the host galaxy (Binney 1977). A strategy for exploring the parameter space of orbits of a population of satellites would be to integrate the orbit of satellites in a fixed non-spherical potential using e.g. Binney's treatment for the dynamics of a point source. In the last years, there have been several studies of how dynamical friction influences the orbit and structure of satellites that go in this direction (e.g. Colpi et al 1999 using the theory of Linear Response), as well as N-body simulations (e.g. van den Bosch et.al. 1999). However there is at present no body of work for this problem against which to compare the analytic treatment, as done for spherically symmetric systems (see for instance Taylor & Babul 2000). Furthermore, mass loss by the satellite is difficult to account for analytically (see Helmi & White 1999; Johnston et al. 1999). In addition, fixed potentials prevent important feed-backs from the dynamical friction process. For example, Weinberg (2000) argues that the wake from a heavy satellite may induce bending modes in the disc. Effects such as wake, disc bending, motion of the primary galaxy's centre of mass, would in turn influence the satellite's orbit.

In this paper, we study how axisymmetric (flattened) DMHs affect the orbital decay and survival of satellites, paying particular attention to the orbital inclination of the satellite with respect to the disc and DMH plane of symmetry. We are motivated by the Holmberg effect, and by the fact that no study of satellite decay exists to date which takes into account both the velocity anisotropy and the flattened density structure of the DMH. Given the likely importance of feedback, and the as yet untested analytical description of dynamical friction in anisotropic systems, we resort to fully self-consistent calculations with live multi-component galaxies and satellites. This has become possible only very recently through the availability of a new algorithm, MaGalie, that allows the construction of large-N flattened multi-component galaxy models (Boily, Kroupa & Peñarrubia 2001, hereinafter BKP).

Section 2 introduces the models. In Section 3 we study how flattened DMHs affect satellite decay, especially in comparison with spherical DMHs without velocity anisotropy. We also touch on orbital precession and its implications for the spread of tidal debris. The paper concludes with Section 4.

2   THE MODELS

A subset of our spherical models are similar to the models of Velázquez & White (1999, hereinafter VW) to facilitate an inter-comparison of different numerical treatments.

2.1   The primary galaxy model

In order to minimize computational time when constructing flattened DMHs with embedded bulges and discs, we apply a new highly-efficient technique using multi-pole potential expansions to tailor the local velocity ellipsoid to the required morphology (BKP). The algorithm to add together individual components in a single galaxy is adapted from Hernquist's method (Hernquist 1993). The new code, MaGalie, scales linearly with particle number and hence we can construct flattened DMHs consisting of $\gtrsim 10^6$ particles or more, in a short computational time.

For the density distributions of the disc we take

$$\rho_d(R,z) = \frac{M_d}{4\pi R_d^2 z_0}\exp(-R/R_d)\text{sech}^2(z/z_0), \tag{1}$$

M_d being the disc mass, z_0 the vertical thickness, and R_d the exponential scale length in the radial direction. The mass profile decays exponentially with R and is composed of isothermal sheets along the vertical direction. Velocities are assumed to have a Gaußian distribution. The square of the radial velocity dispersion is taken to be proportional to the surface density (see Lewis & Freeman 1989), $\overline{v_R^2} \propto \Sigma(R) = \Sigma(0)\exp(-R/R_d)$, where the constant of proportionality is determined by fixing Toomre's Q-parameter at the Solar radius. Following VW, we select $Q_\odot = Q(R_\odot) = 1.5$. The vertical component of the velocity ellipsoid is $\overline{v_z^2} = \pi G\Sigma(R)z_0$ in agreement with an isothermal sheet (Spitzer 1942). The azimuthal component is obtained from the epicyclic approximation $\sigma_\phi^2 = \overline{v_R^2}\kappa^2/(4\Omega^2)$ (e.g. Binney & Tremaine 1987, hereinafter BT).

For the bulge we adopt the spherical Hernquist profile (Hernquist 1990),

$$\rho_b = \frac{M_b}{2\pi}\frac{a}{r(r+a)^3}, \tag{2}$$

where M_b is the bulge mass and a the spherical scale length. This analytical profile fits the de Vaucouleurs law (de Vaucouleurs 1948). The velocity field is constructed from the Jeans equations by assuming isotropic Gaussian velocity distributions at each radial distance (Hernquist 1993).

We use a non-singular isothermal profile for the DMH,

$$\rho_h = \frac{M_h\alpha}{2\pi^{3/2}r_{\text{cut}}}\frac{\exp(-r^2/r_{\text{cut}}^2)}{r^2+\gamma^2}, \tag{3}$$

M_h being the DMH mass, r_{cut} the cut-off radius and γ the core radius, and

$$\alpha \equiv \{1 - \sqrt{\pi}\beta\exp(\beta^2)[1-\text{erf}(\beta)]\}^{-1} = \tag{4}$$
$$1 + \sqrt{\pi}\beta + (\pi-2)\beta^2 + O(\beta^3)$$

where $\beta = \gamma/r_{\text{cut}} \lesssim 1/24$ in our calculations. For $\beta = 1/24$ we find $\alpha \simeq 1.076 \rightarrow 1$ already and hence thereafter we set $\alpha = 1$ in our analysis. To construct the flattened (oblate) DMHs, a non-homologous transformation is applied to (3) to achieve the desired axis ratio c/a while preserving the central density: 1) first we flatten the DMH down the z-axis only, until the desired aspect ratio $q_h = c/a$ is reached; 2) then all axes are stretched by a factor λ, $A = \lambda R$, such that $M/R^3 = M/A^2C = M/[A^3q_h] = M/[R^3\lambda^3q_h]$. Solving for $\lambda = q_h^{-1/3} \approx 1.18$ when $q_h = 0.6$. The orbital period $\propto 1/\sqrt{G\rho}$, and hence the dynamical time, is unchanged in the new equilibrium. Particle velocities are obtained by adjusting the initial isotropic distribution (as for the bulge) to
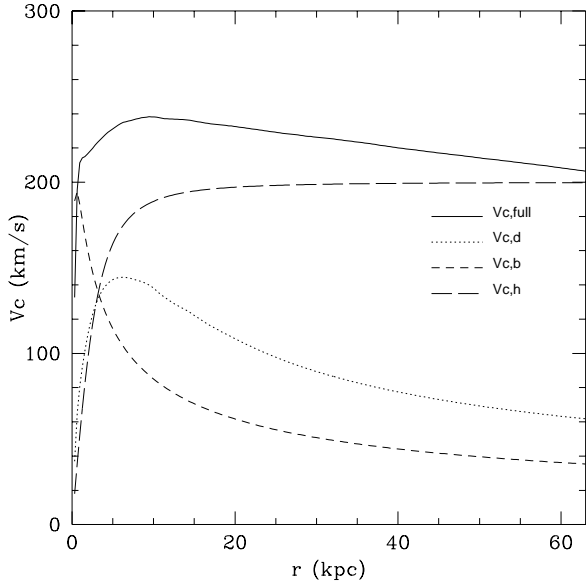
Figure 1. Total contribution from the three G1 galaxy components (disc, bulge and halo) to the circular velocity (solid line). We also plot the circular velocity for each galaxy component. On very small scales ($r < 1$ kpc) the bulge accounts for the bulk of V_c. Further out, the dynamics is dominated by the halo. The solar radius is at $R_\odot = 8.5$ kpc.

the oblate iso-potential surfaces leading to a stable axisymmetric DMH with embedded bulge and disc (BKP).

We use four different isothermal DMH models: a spherical (G1) and a flattened DMH (G2) with axis-ratio $q_h = c/a = 0.6$, which lies within the distribution of flattenings given by CDM models. The third (G3) and fourth (G4) models have the same properties as G1 and G2, respectively, but with enlarged cut-off radii. We can define two typical distances, the core radius in the symmetry plane (γ_a) and in the vertical direction (γ_c). Since concentric iso-density contours have the same axis-ratio throughout the DMH, both core radii are related by $q_h = \gamma_c/\gamma_a$.

Our system of units is such that $M_d = R_d = 1$ and $G = 1$. According to Bahcall, Smith & Soneira (1982), $M_d = 5.6 \times 10^{10} M_\odot$ and $R_d = 3.5$ kpc for the Milky Way which we adopt as a typical primary galaxy model, so that time and velocity units are, respectively, 1.3×10^7 yr and $262 \, \mathrm{km s}^{-1}$. The half-mass radius of the disc is located at $R_{0.5} \sim 1.7 R_d = 5.95$ kpc, with a rotation period of 13 time units. Table 1 summarizes the parameters and Fig. 1 plots rotational curves for two models.

As VW point out, there are some caveats to keep in mind concerning the above models: (i) The DMHs are possibly too small in mass and extension. Zaritsky & White (1994) show, by studying satellite orbits in the Local Group and external galaxies, that DMH limits may extend beyond 200 kpc with masses over $2 \times 10^{12} M_\odot$. However, as VW comment, the velocity curves of our DMHs G1 and G2 are consistent with the largest velocities observed for stars in the solar neighbourhood (Carney & Lathman 1987), and they are possibly massive enough to give realistic velocities of satellites on eccentric orbits. (ii) The DMHs may be too concentrated. Persic, Salucci & Stel (1996) argue for a DMH core radius of $\gamma = (1 \rightarrow 2) \times R_{opt}$, $R_{opt} = 3.2 R_d$, where R_d is the disc scale-length. However the DMH parameters were selected to avoid bar formation in the disc. We observed that a less concentrated DMH or bulge allows a stable disc

	Symbol	Value(ph.u)	Value (m.u)
Disc	N_d	100000	
	M_d	$5.60 \times 10^{10} \mathrm{M}_\odot$	1.00
	R_d	3.50 kpc	1.00
	z_0	1.40 kpc	0.40
	$Q_\odot$	1.50	1.50
	$R_\odot$	8.50 kpc	2.43
Bulge	N_b	33328	
	M_b	$1.87 \times 10^{10} \mathrm{M}_\odot$	1/3
	a	0.53 kpc	0.15
DMH (G1) (spherical)	N_h	1400000	
	M_h	$7.84 \times 10^{11} \mathrm{M}_\odot$	14.00
	γ	3.50 kpc	1.00
	q_h	1.00	1.00
	r_{cut}	84.00 kpc	24.00
DMH (G2) (oblate)	N_h	1400000	
	M_h	$7.84 \times 10^{11} \mathrm{M}_\odot$	14.00
	q_h	0.60	0.60
	γ_a	3.80 kpc	1.10
	γ_c	2.28 kpc	0.65
	r_{cut}	84.00 kpc	24.00
DMH (G3) (spherical)	N_h	1400000	
	M_h	$7.84 \times 10^{11} \mathrm{M}_\odot$	14.00
	γ	3.50 kpc	1.00
	q_h	1.00	1.00
	r_{cut}	133.00 kpc	38.00
DMH (G4) (oblate)	N_h	1400000	
	M_h	$7.84 \times 10^{11} \mathrm{M}_\odot$	14.00
	q_h	0.60	0.60
	γ_a	3.80 kpc	1.10
	γ_c	2.28 kpc	0.65
	r_{cut}	133.00 kpc	38.00

Table 1. Primary galaxy models. Oblate models have an aspect ratio $q_h = 0.6$. The units are such that Ph.u. means 'physical units', and m.u. 'model units'.

to form a bar after few satellite passages. With our γ, the presence of a bar is avoided at least until the destruction of the satellite.

2.2 Satellite models

We use self-consistent King models (King 1966) to represent our dwarf galaxies. These models fit early-type dwarf galaxies (Binggeli et al. 1984), where r_c and r_t are the core and tidal radii, respectively. For a comparison with the work of VW we adopt $c = 0.8$.

To construct the models we choose the satellite mass M_s, r_c, r_t and thus c. The tidal radius is determined by computing the density contrast, $\rho_s(r_t)/\overline{\rho_g}(r_a) \sim 3$, at the apo-centric distance ($r_a = 55$ kpc) at $t = 0$, $\overline{\rho_g}(r)$ being the averaged density of the galaxy (same procedure as VW). This guarantees that all satellite particles are bound

	Symbol	Value(ph.u)	Value (m.u)
S1	N_s	40000	
	M_s	$5.60 \times 10^9 \mathrm{M_\odot}$	0.10
	$\Psi(0)/\sigma_0^2$	5.00	5.00
	r_c	1.00 kpc	0.29
	r_t	6.31 kpc	1.80
	c	0.80	0.80
	$<r>$	1.64 kpc	0.47
	σ_0	$52.00 \mathrm{kms}^{-1}$	0.20
S2	N_s	40000	
	M_s	$1.12 \times 10^{10} \mathrm{M_\odot}$	0.20
	$\Psi(0)/\sigma_0^2$	5.00	5.00
	r_c	1.00 kpc	0.29
	r_t	6.31 kpc	1.80
	c	0.80	0.80
	$<r>$	1.64 kpc	0.47
	σ_0	$74.00 \mathrm{kms}^{-1}$	0.28

Table 2. Satellite models. $\Psi(0) = \Phi(r_t) - \Phi(0)$, $\Phi(0)$ being the central potential and $\Phi(r_t)$ the potential at the tidal radius (following BT notation); σ_0 is the velocity dispersion at the centre, and $<r>$ the average radius of the satellite.

Figure 2. Rotational curve of the satellite models S1 and S2 (see Table 2 for the characteristics of each one).

at $t = 0$. Tables for the numerical rendition of the corresponding King profiles can found in BT or in the original paper of King (1966). Table 2 summarizes the parameters, while Fig. 2 plots rotational curves. Note that we use the same M_s, r_c and "r_t" despite placing the satellites at different apogalactica $r_a \geq 55$ kpc (Section 2.3), which increases the true tidal radius of the satellite, though the stability condition at $t = 0$ is still well-accomplished. We do this rather than using different r_c or r_t in order to study the same satellites on different orbits.

Our satellites are much more massive than the Milky Way dSph satellites which have $M_s \lesssim 10^8 \, M_\odot$, but our adopted values are typical for the satellites that enter distant samples such as used by Holmberg (1969) and Zaritsky & González (1999).

2.3 Numerical method and orbital parameters

We use SUPERBOX (Fellhauer et al. 2000) to evolve the galaxy-satellite system. SUPERBOX is a highly efficient particle mesh-code based on a leap-frog scheme, and has been already implemented in an extensive study of satellite disruption by Kroupa (1997) and Klessen & Kroupa (1998).

Our integration time step is 0.39 Myr which is about 1/25th the dynamical time of satellite S2. We have three resolution zones, each with 64^3 grid-cells: (i) The inner grid covers out to 3 radial disc scale-lengths, which contains $\approx$ 90 % of the disc mass, providing a resolution of 350 pc per grid-cell. (ii) The middle grid covers the whole galaxy, with an extension of 24 disc scale-lengths (84 kpc) for the models G1 and G2, giving a resolution of 2.8 kpc per grid-cell. The satellite always orbits within this grid except when it reaches the disc, avoiding cross-border effects (see Fellhauer et al. 2000). For the models G3 and G4, the middle grid extends to 141 kpc and has a resolution of 4.7 kpc per grid-cell. The orbits of the satellites are located within this zone. (iii) The
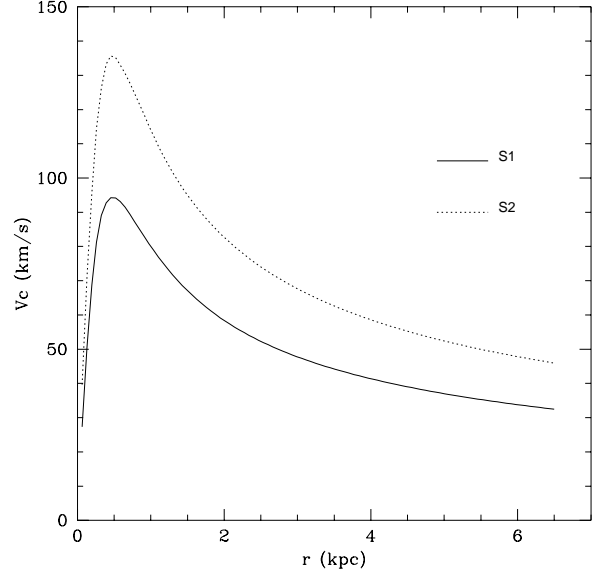
outermost grid extends to 348 kpc and contains the local universe, at a resolution of 11.6 Kpc.

As for the satellite grid-structure, the resolutions are 816 pc per grid-cell for the inner grid that extends to 24.48 kpc, 1.2 kpc per grid-cell for the middle grid which extends to 36 kpc, and 11.6 kpc per grid-cell for the outermost grid that covers the local universe. Only the inner and middle grids move along with the satellites, remaining positioned on their centre-of-density locations. The outer grid is identical for primary galaxy and satellite.

Klessen & Kroupa (1998) compared calculations performed with SUPERBOX with direct-integration N-body calculations and found good agreement. Specifically, they verified that varying the grid resolution by factors of a few did not lead to unstable satellite models. The stability of the satellite models does not depend strongly on the values adopted here. Furthermore, based on the comparison with the direct-integration method, the heating introduced by two-body effects prove entirely negligible for the model satellites we consider. The selection of grid parameters ensures the conservation of energy and angular momentum for satellites in isolation over times as long as our calculations to a high degree. Conservation of total energy and angular momentum is better than 1% for all the models.

The disc is poorly resolved in the z–direction and we do not study its evolution in any detail. We verified that the disc parameters do not evolve for galaxies in isolation (no satellites). Since SUPERBOX is a mesh code, a poor z-resolution for the disc is expected due to the limited number of grids. This provokes the disc modeled here to be unrealistically thick, however it does provide a quadrupolar (non-spherical) potential of the appropriate magnitude. A mesh code has the advantage that it does not introduce self-heating since it does not calculate two-body interactions, which would have been significant in the disc given the finite number of particles used (see the discussion in VW). The effects on the satellite dynamics due to two-body interactions are drastically reduced by the low mass of the

halo particles (see Steinmetz & White 1997). Furthermore the disc heating by halo particles is minimized since each component particle masses are in a one-to-one ratio.

The decay of satellites with various masses through dynamical friction in an extended spherical DMH is studied by Fellhauer et al. (2000), who found good agreement between SUPERBOX calculations and Chandrasekhar's (1960) formula for dynamical friction when the Coulomb logarithm Λ is set to $\ln \lambda = 1.6$ (cf. eq 5 below). This agrees with the findings by VW for similar calculations.

We carry out a set of calculations varying the parameters of the satellite and the primary galaxy that influence the satellite–primary galaxy interaction. These parameters are: (i) the initial orbital inclination (θ_i), defined as the angle between the initial angular momentum vector of the satellite and the initial angular momentum of the disc, (ii) the satellite's mass, (iii) the satellite's apo-galactic distance, (iv) its orbital eccentricity, and (v) the DMHs ellipticity, $1 - q_h$.

Before injecting the satellite into the primary galaxy we allow the galaxy and satellite to settle into a stationary state by integrating the isolated systems for a few dynamical times with SUPERBOX (as in Kroupa 1997). Examples of the stationarity of multi-component galaxies are given in BKP. The satellite is then placed at apo-galacticon with a velocity as described next.

The orbit of the satellites are rosettes. VW define the 'circularity' of the orbit as $\epsilon_J \equiv J/J_C(E)$, J being the satellite's angular momentum and J_C the corresponding angular momentum for a circular orbit with the same energy E as the satellite's orbit. In practice, we take the circular velocity from the rotational curve plotted in Fig. 1 at the satellite's initial distance, and multiply it by ϵ_J. This procedure gives an eccentric orbit with the same energy. The parameters of the numerical experiments are listed in Table 3.

3 SATELLITE DECAY

We discuss our results in general terms below before going into detailed consideration of the mass loss and survival of satellites (Section 3.2), and the orbital evolution of the inclination angle, eccentricity and precession, respectively (Sections 3.3 to 3.5). Section 3.6 takes a brief look at the implications for tidal streams of dissolving satellites.

3.1 Introductory comments

We denote by 'G1S145' the compound primary galaxy made, in this case, of a spherical DMH plus embedded disc and bulge, G1, and satellite S1, in an orbital plane initially set at an inclination angle $\theta = 45°$ with respect to the plane of symmetry of the system. In what follows we take this model as reference, but all models followed a similar evolution.

There are two main physical mechanisms that regulate the satellite's orbital decay: (i) dynamical friction from the disc, bulge and DMH, and (ii) tidal interactions, causing internal heating and mass loss. The evolution of the satellite's orbital radius and mass profile highlight the basic characteristics of these two processes. Dynamical friction causes a steady decrease of the satellite's apo- and peri-centres in time as shown on Fig.3 (dotted line). (Lengths are given in model units on the figure but the time is in Gyr.) From $t = 0$

Name	Gal. model	Sat. model	θ_i	e	r_p [kpc]	r_a [kpc]
G1S100	G1	S1	0°	0.7	17	55
G1S1180	G1	S1	180°	0.7	17	55
G1S145	G1	S1	45°	0.7	17	55
G1S1135	G1	S1	135°	0.7	17	55
G1S190	G1	S1	90°	0.7	17	55
G2S100	G2	S1	0°	0.7	17	55
G2S115	G2	S1	15°	0.7	17	55
G2S130	G2	S1	30°	0.7	17	55
G2S145	G2	S1	45°	0.7	17	55
G2S160	G2	S1	60°	0.7	17	55
G2S190	G2	S1	90°	0.7	17	55
G2S1135	G2	S1	135°	0.7	17	55
G1S100e	G1	S1	0°	0.45	30	55
G1S190e	G1	S1	90°	0.45	30	55
G2S100e	G2	S1	0°	0.45	30	55
G2S190e	G2	S1	90°	0.45	30	55
G1S100c	G1	S1	0°	0	55	55
G1S145c	G1	S1	45°	0	55	55
G1S190c	G1	S1	90°	0	55	55
G2S100c	G2	S1	0°	0	55	55
G2S190c	G2	S1	90°	0	55	55
G1S200	G1	S2	0°	0.7	17	55
G1S245	G1	S2	45°	0.7	17	55
G1S290	G1	S2	90°	0.7	17	55
G2S200	G2	S2	0°	0.7	17	55
G2S245	G2	S2	45°	0.7	17	55
G2S290	G2	S2	90°	0.7	17	55
G3S200	G3	S2	0°	0.8	20	110
G3S245	G3	S2	45°	0.8	20	110
G3S290	G3	S2	90°	0.8	20	110
G4S200	G4	S2	0°	0.8	20	110
G4S245	G4	S2	45°	0.8	20	110
G4S290	G4	S2	90°	0.8	20	110

Table 3. The numerical experiments. The peri- and apo-galactica are r_p and r_a, respectively, and $e = 1 - r_p/r_a$ is the orbital ellipticity (BT, p.21).

and until $t < 2$Gyr, both quantities, apo- and peri-centres, decrease monotonically. When $t > 2$ Gyr, the orbital radius $r \approx 5$ or smaller, and the orbital decay is not monotonic anymore. The proximity to the disc means that non-radial forces affect strongly the remaining evolution, along with the structure of the satellite.

To measure changes in the structure of the satellite, we plotted the ten-percentile Lagrange radii centred on the density maximum of the satellite (Fig.3, solid lines). At $t \approx 3$ Gyr, the galactic tidal field has inflated the satellite to the extent that half of its initial mass is spread throughout the volume circumscribed by its orbit. We note that the inner 10 per cent Lagrange radius is largely unaffected until the very late stages of integration. Our strategy for determining the orbital parameters of the satellite therefore consisted in locating the position of the density maximum of the inner-
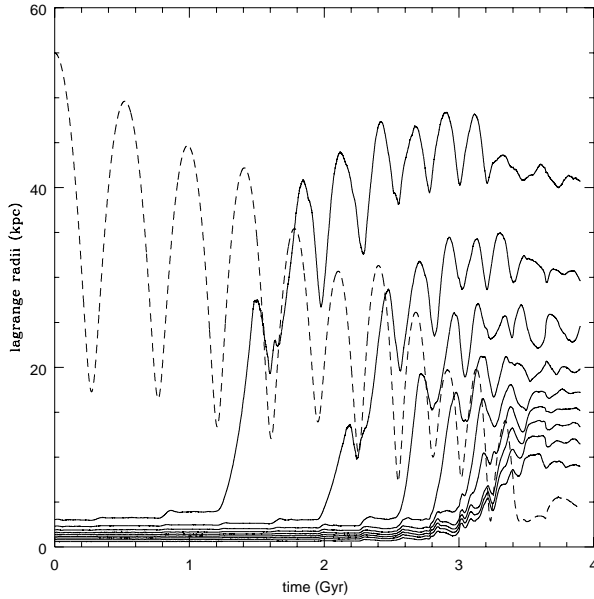
Figure 3. Evolution of the satellite's Lagrange radii (solid curves, defined as the radius at which the spherically enclosed mass amounts to 10%, 20%....,90%) for the model G1S145. The dotted line represents the distance of the satellite's centre of density to centre of the primary galaxy. Distances are in model units. The overall evolution is similar in all other models (Table 3).

most Lagrange radius, which then defines a reference coordinate.

3.2 Mass loss and disruption times

To calculate the mass remaining bound to the satellite, $M_s(t)$, we compute the potential energy $\Phi_i < 0$ of each satellite particle presumed bound to the satellite, and its kinetic energy (T_i) in the satellite frame. Following VW, particles with $E_i = T_i + m_s(\Phi_i + \Phi_{ext}) > 0$ are labeled unbound, where m_s is the mass of one satellite particle. Particles with $E_i > 0$ are removed and the procedure repeated until only negative energy particles are left. $\Phi_{ext} = GM_g(r < r_s)/r_s > 0$ is the external potential from the primary galaxy at the satellite's centre-of-density (r_s). All the particles of the satellite are thus assumed to feel the same external potential, which is a useful and sufficiently accurate approximation, taking into account that most of the bound particles are located very close to this point. For example, in Fig. 3 most of the satellite's mass lies at a distance less than 4 kpc from the position of the centre-of-density until the satellite's disruption. This approximation fails whenever the satellite's size is comparable to its distance to the galaxy centre.

Satellites lose mass due to the galaxy's tidal forces. The mass loss happens mostly at perigalacticon, since the gradient of the galaxy's gravitational force reaches a maximum at that point (see Fig. 3). This is seen indirectly in the oscillations of Lagrange radii, always in phase with the orbit of the satellite: the satellite fills its Roche lobe and consequently responds strongly to the changing tidal field. Thus a decrease of the apo-galacticon distance implies an enhanced
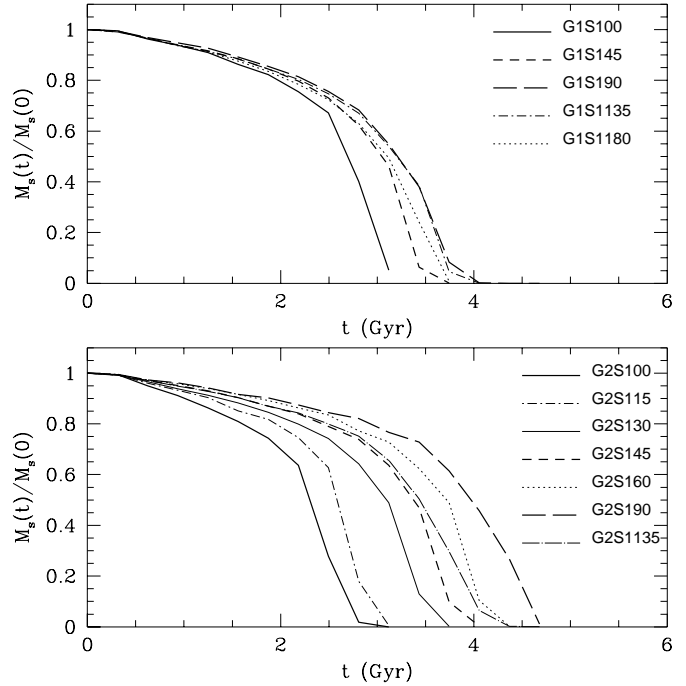

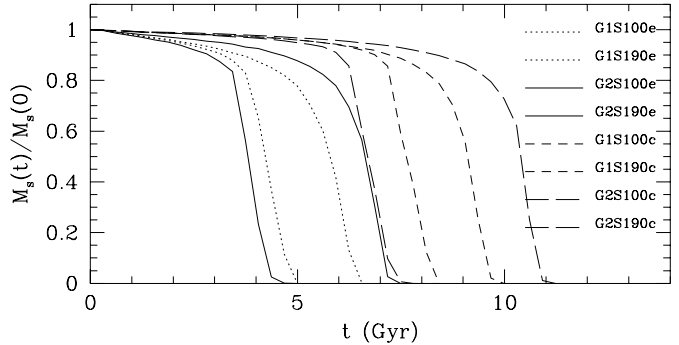**Figure 4. a:** Evolution of the satellite mass for $M_s = 0.1 M_d$ and eccentricity $e \simeq 0.7$.

Figure 4 – *continued* **b:** As Fig. 4a for satellites with $M_s = 0.1 M_d$ and initial eccentricity $e \simeq 0.45$ and $e = 0$. (Note that the time-axis has changed scale.)

mass loss. The evolution of satellites exposed to strongly varying tidal fields is discussed at length by Piatek & Pryor (1995) for one perigalactic passage, whereas long-term satellite harassment is addressed by Kroupa (1997) and Klessen & Kroupa (1998). Consequently, we will not study the internal evolution of the satellites apart from the bound mass fraction.

3.2.1 Satellites with $M_s = 0.1 M_d$

Fig. 4 shows the evolution of the satellite mass for different initial orbital inclinations for satellites with $M_s \equiv M_s(0) = 0.1 M_d$ and eccentricity $e \simeq 0.7$. From this figure we can assert that: (i) The satellites are disrupted completely at about the same time they reach the galactic disc (Fig. 3). (ii) For all the models, the survival time is, at least, 1 Gyr (25%) longer than the equivalent simulations of VW (upper panel of Fig. 4a). We consider this difference to be indicative of
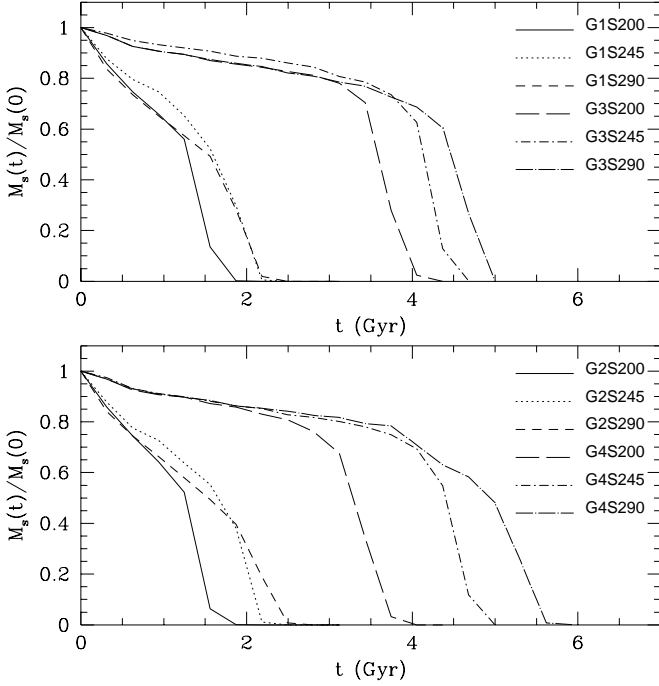
Figure 4 – *continued* **c:** As Fig. 4a for satellites with $M_s = 0.2 M_d$. (Note that the time-axis has changed scale.)

the uncertainty intrinsic to methods that approximate collisionless dynamics. The difference comes about, in part, due to different numbers of particles, but also due to the spatial resolution of the method. Prugniel & Combes (1992) and Whade & Donner (1996) find that dynamical friction is artificially increased due to numerical noise if the particle number is small. Similar differences were also noted in the computations by Klessen & Kroupa (1998) of satellite harassment using different codes. However, we observe that the range of disruption times for our models G1S1 (as used by VW) is approximately the same, indicating that disc effects are well reproduced by our code and giving confidence to the following results we obtain using flattened DMHs. (iii) Flattened DMHs spread the range of disruption times. In Fig. 4a we can see that, for satellites with $M_s = 0.1 M_d$ embedded within spherical DMHs this range is ~ 0.9 Gyr (upper panel), polar satellites having the longest survival time. For satellites with the same mass but within flattened DMHs the range grows to ~ 1.9 Gyr (lower panel). (iv) Satellites with a high orbital inclination within flattened DMHs have longer survival times than satellites within spherical DMHs with the same initial orbit. For instance, taking the polar satellite as the extreme case, G2S190 survives $\sim 0.6 - 1$ Gyr longer than G1S190. (v) Satellites with low orbital inclination suffer the contrary effect: those within spherical DMHs survive longer than those within flattened DMHs. Taking the prograde and coplanar orbit as the extreme case, G1S100 survives ~ 0.4 Gyr longer than G2S100.

In Fig. 4b we compare polar and coplanar satellites within flattened and spherical DMHs with orbital eccentricity $e \approx 0.45$ and 0 to obtain an indication of the dependency of the life-time on e (orbits with intermediate inclination also have intermediate survival times, Fig. 4a). As expected, less eccentric orbits lead to longer survival times, since the perigalactic distance is larger and, moreover, tidal
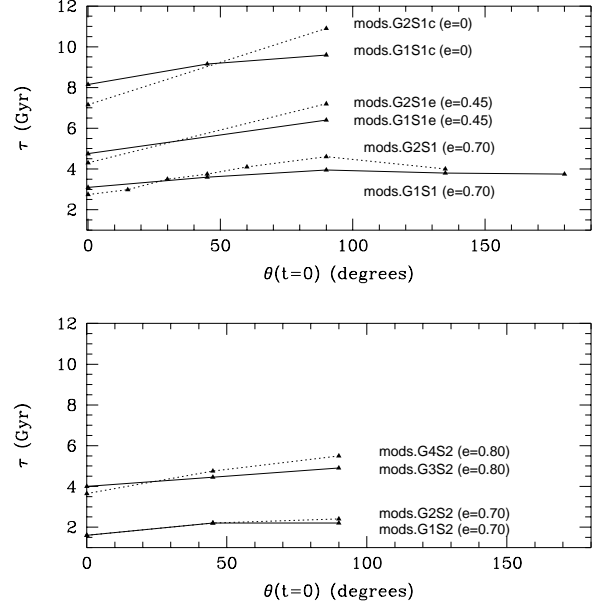

Figure 5. The time τ when the satellite mass reaches 10 per cent of its initial value, $M_s(\tau) = 0.1 M_s$, is plotted vs the initial orbital inclination. Upper panel is for satellite models S1 in primary galaxies G1 and G2, whereas the lower panel shows the results for satellites S2. Note that in all cases τ increases with increasing $\theta < 90°$ for galaxies embedded in a spherical and a flattened DMH, due to dynamical friction on the disc. The effect of this is particularly nicely seen from the different slopes, $d\tau/d\theta$, for prograde ($\theta = 0 - 90°$) and retrograde ($\theta = 90 - 180°$) orbits. The increase is significantly larger for satellites orbiting in flattened DMHs, and becomes larger for decreasing orbital eccentricity (Table 4) and decreasing satellite mass, which allows longer coupling of the satellite to the anisotropic velocity field in the DMH.

forces are weaker. Furthermore, the survival times show a larger spread. Less eccentric orbits survive longer, so that anisotropic dynamical friction has a longer time to act. We can see that coplanar satellites within a spherical DMH (model G1S100e) survive ~ 0.6 Gyr longer than a coplanar satellite within a flattened DMH (model G2S100e), while the survival time of a polar satellite within a spherical DMH (model G1S190e) is ≈ 1 Gyr shorter than the corresponding satellite in the flattened DMH (model G2S190e). Thus, the range of survival times increases from about 1.5 Gyr to 3 Gyr. This range becomes even larger for circular orbits.

This state of affairs is summarized in Fig. 5 for all satellite models, whereas Table 4 compares the decay times for S1 satellites in dependence of the orbital eccentricity and inclination. The table nicely shows that the survival time increases significantly with decreasing eccentricity. It also shows that oblate DMHs lead to consistently larger differences, $\Delta\tau$, between the decay times for polar and coplanar orbits, $\Delta\tau$ consistently being approximately 100 per cent larger in flattened DMHs than in spherical DMHs ($\Delta\tau_{\rm obl} \approx 2\,\Delta\tau_{\rm sph}$). This is the key result of this study.

3.2.2   Satellites with $M_s = 0.2 M_d$

The temporal evolution of satellite masses with $M_s = 0.2 M_d$ is shown in Fig. 4c. There are no significant differences in

model	$e(t=0)$	$\tau_0 \equiv$ $\tau(\theta=0)$ [Gyr]	$\tau_{90} \equiv$ $\tau(\theta=90)$ [Gyr]	$\Delta\tau \equiv$ $\tau_{90} - \tau_0$ [Gyr]
G2S1c(obl)	0	7.0	11.0	4.0
G1S1c(sph)	0	8.0	9.6	1.6
G2S1e(obl)	0.45	4.3	7.3	3.0
G1S1e(sph)	0.45	4.8	6.5	1.7
G2S1(obl)	0.7	2.7	4.6	1.9
G1S1(sph)	0.7	3.1	4.0	0.9

Table 4. Summary of decay times for satellite models S1 ($M_s = 0.1\,M_d$) in oblate (obl) and spherical (sph) DMHs with different initial orbital eccentricity e and orbital inclination θ. τ_0 is the decay time when the satellite that is initially on an orbit with inclination $\theta = 0^\text{o}$ has lost 90 per cent of its mass, whereas τ_{90} is the decay time for polar orbits ($\theta = 90^\text{o}$).

survival times for satellites in spherical and flattened DMHs if $r_a = 55$ kpc. At the same time, the dependency on the inclination decreases, causing the range to be narrower in both cases. The cause is the fast decay of the satellites, so that the anisotropy of the DMH's velocity dispersion does not have enough time to act. To better assess this, we introduce a set of computations selecting larger initial apo-galactic distances (models G3 and G4). The cut-off radius of the Galaxy is increased, which changes the rotational curve (see Fig. 1). The results are also plotted in Fig. 4c. A similar spread of survival times as for models with $M_s = 0.1\,M_d$ and 'G2' flattened DMHs becomes evident; the range of disruption times for spherical (G3) and flattened DMHs (G4) are, respectively, ~ 1 and ~ 2 Gyr.

The results concerning the disruption times seen on Fig. 4c between small and large DMHs (G1/G3 and G2/G4 pairs displayed on Fig.4c, bottom panel) are related to one another as follows. DMHs G3 and G4 have the same mass as G1 and G2, but are more extended by a factor $\eta = 133\,\text{kpc}/84\,\text{kpc} = 1.58$ (Table 1). This implies that the dynamical time-scale ($\propto 1/\sqrt{G\rho}$), i.e. the periods of satellites on equivalent orbits, are longer in haloes G3 and G4 by a factor $\sqrt{\rho(G2)/\rho(G1)} = 1.58^{3/2} = 2$. Orbits in G3 and G4 equivalent to those in G1 and G2, respectively, are orbits with semi-major axes extended by η in a homologous mapping of the systems. Our satellite orbits, however, have apo-galactic distances in G3 and G4 twice as large as in DMHs G1 and G2. The orbital times of models G3S2nn and G4S2nn are in total $1.58^{3/2} \times 2/1.58 = 2 \times 2/1.58 \approx 2.5$ times longer than models of satellites in DMHs G1 and G2. This is approximately what we observe from comparing the curves on Fig. 4c with DMHs G1/G3 or G2/G4.

On the top panel of Fig. 4c, the time when $M(t)/M(0) \approx 0.10$ is $t \approx 2$ Gyrs for all G1 models. If the homologous transformation applied strictly, the curves for the G2 halo models should approach 5 Gyrs when $M(t)/M(0) = 1/10$. The fact that they are spread between 4 and 5 Gyrs, and thus deviate from the homologous map, indicates that the disc and bulge, which were left unchanged, play an important role in the mass decay rate of the satellites. Furthermore, the spread in destruction times between models is a

factor ≈ 2, from 1 Gyr (G1 models) to 2 Gyr (G3 models), suggesting that the time-scales for orbital decay are controlled by the DMH, while the combined tidal field of the disc and bulge contributes mainly to mass stripping. Similar conclusions would apply for the G2/G4 models shown on the bottom panel of the figure.

3.2.3 Prograde versus retrograde orbits

Results for models with spherical DMHs may be divided into two according to whether the orbit of the satellite is aligned with the disc's angular momentum vector (prograde) or anti-aligned (retrograde). Keeping the initial satellite velocity vector unchanged, a prograde orbit is found for an initial orbital inclination angle $0^\circ < \theta < 90^\circ$, and retrograde orbits in the cone $90^\circ < \theta < 180^\circ$.

Table 3 lists four models with spherical G1 DMHs and ellipticity $e = 0.7$ (top segment in the Table). Models G1S100 and G1S1180 are respectively prograde and retrograde with respect to the disc, but are otherwise identical. From Fig. 4a (top panel) we find for these two simulations a 90% mass-loss after ≈ 3 Gyr and 3.5 Gyr, respectively, an increase of nearly 20% ; a similar conclusion applies for models G1S145 and G1S1135. These findings are qualitatively similar with those of VW: (i) Satellites on prograde orbits lose angular momentum faster than their retrograde counterparts, leading to more rapid decay. (ii) Polar orbits have a similar decay rate as retrograde orbits, as found from comparing model G1S190 and G1S1135, Fig 4a. This implies that our treatment of the live disc captures the essential physics relevant for this work.

Figure 5 summarizes the findings for decay rates for the simulations performed. Point (i) above also applies to flattened DMHs. However, Fig. 5 suggests in this case that the difference in decay rates between prograde and retrograde orbits is reduced by about 80 % for flattened DMHs.

For spherical DMHs the above results can be understood partially by considering Chandrasekhar's expression (Chandrasekhar 1960) for dynamical friction,

$$\mathbf{F}_{\mathrm{df}} = -\frac{4\pi G^2 M_s^2(t)\rho(<v_s)\ln\Lambda}{\Delta v^3}\mathbf{v}_s, \tag{5}$$

$\Delta v = |\vec{v_s} - \vec{v_m}|$ being the relative velocity between the satellite and the disc particle background, v_m is the disc particle velocity and $\rho(<v_s)$ the density calculated only for those particles with velocity less than the satellite's velocity v_s, and $\ln\Lambda$ the Coulomb logarithm, defined as $\Lambda = p_{\max}/p_{90}$. In this expression, $p_{\max}$ is the maximum impact parameter (conventionally taken as the half-mass radius of the system), and p_{90} the minimum impact parameter. Since these quantities are not well defined, the Coulomb logarithm remains, to a certain degree, an adjustable parameter. Recent self-consistent computations with different N-body codes leads to $\ln\Lambda = 1.5 \rightarrow 2$ (VW; Fellhauer et al. 2000).

The different decay rate between prograde orbits and their retrograde counterparts is caused, in part, by the disc's dynamical friction when the satellite is near perigalacticon. Retrograde orbits have a much higher relative velocity Δv due to the disc's rotation and, therefore, they suffer a smaller drag force. The bulge or the DMH's dynamical friction make no differences since both are non-rotational and spherical, which also explains the small differences of decay rates be-

tween the polar and the retrograde case (in both cases dynamical friction through the disc can be neglected compared to the DMH's dynamical friction). In addition to dynamical friction, resonances between the satellite and the disc influence the orbital decay, but a detailed analysis goes beyond the aim of this work. As for the different decay rates depending on the satellite's mass, the dynamical friction force varies with M_s^2, so that satellites with $M_s = 0.2\,M_d$ suffer a four times larger friction force than those with $M_s = 0.1\,M_d$.

3.3 The orbital inclination θ

Binney (1977) extended the dynamical friction force (5) to non-isotropic velocity fields. He showed how anisotropic friction leads to orbit alignment with the velocity ellipsoid plane of symmetry of the host galaxy. Here disc and DMH spheroids define a unique $z = 0$ plane of symmetry, common to both mass distribution and velocity ellipsoid. We may, therefore, anticipate enhanced satellite orbit alignment relatively to Binney's analysis, due to the non-uniform, aspherical mass profile.

In Fig. 6 we graph the time-evolution of the direction angle θ for a set of simulations with oblate G2 DMHs ($q_h = 0.6$) and S1 satellites (solid lines on the figure) as well as two reference runs with spherical G1 DMHs (dotted lines on the figure).

The average of the orbital inclination $\theta(t)$ decreases monotonically in time for satellites orbiting in flattened DMHs which have initially $\theta \neq 0°$ or $90°$. The decrease in $\theta(t)$ is more appreciable for smaller values of $\theta(0)$. This is seen for instance by comparing the curves with $\theta(0) = 15°$ and $30°$ to the solutions with $\theta(0) = 60°$ and $90°$. For the latter, polar orbit, no decay of $\theta(t)$ is observed for the duration of the integration, whereas for the $\theta(0) = 15°$ case the orbit aligns fully with the plane of symmetry of the system (coincident with the disc of the host galaxy).

By contrast, satellites orbiting in spherical DMHs show little or no decay of $\theta(t)$, for all initial values of θ (dotted lines, Fig. 6). This clearly indicates that the anisotropic DMH, and not the disc, drives most of the orbital evolution and alignment, since in all cases a galactic disc is present.

The figure also reveals periodic oscillations of $\theta(t)$ for satellites on inclined orbits, of frequency approximately in tune with the satellites' orbital motion. Inspection of the figure shows this to be the case for systems with either spherical or flattened DMHs. Note that no such oscillations in $\theta(t)$ is observed for polar or co-planar orbits. We examine the origin these oscillations, distinguishing two phases of time around $t = 2$ Gyrs.

For $0 < t < 2$Gyr the satellites orbital radius $r_s \gg R_d$. Over this interval of time, the orbits are such that those obtained for flattened DMHs lead to much larger oscillations in $\theta(t)$ compared with the solutions with spherical DMHs. We therefore attribute these oscillations to torques from the DMH acting on the satellites

$$\mathbf{\Gamma} = \mathbf{r} \times \nabla\Phi = R\left(\frac{\partial\Phi}{\partial z} - z\frac{\partial\Phi}{\partial R}\right)\mathbf{e}_\phi$$

which by symmetry arguments must lie in the plane of the axi-symmetric galaxy. The torque Γ is positive or negative according to the phase of the orbit.

For $t > 2$Gyr the situation is similar for all calculations,

independently of the morphology of the DMH. Thus the oscillations we observe clearly for flattened-DMH orbits are now noticeable for the solutions with spherical DMHs, too. In this phase of evolution, $r_s \sim R_d$ or less so that the disc potential contributes most of the force felt by the satellite and hence the torque Γ acting on it. At this stage, a coupling between the disc response and the satellite motion is expected: we observed that these oscillations are highly softened in calculations with a static disc and bulge. Since the orbital angular momentum $L \approx r_s v_s m_s$ and $\Delta L = \Gamma dt \approx r_s G\Sigma(r_s/v_s)$, where Σ is the disc's surface density, both L and the angular momentum accrued ΔL over one revolution will be of comparable magnitude if $v_s^2 \sim GM_d/r_s$, i.e. when the disc potential is the predominant contributor to the force acting on the satellite. The direction angle $\theta(t)$ varies therefore wildly towards the end of the simulations in all cases save the coplanar $\theta(0) = 0°$ one, for which $\Gamma = 0$ at all times.

The oscillations or periodic fluctuations we have discussed are subject to enhancements owing to our choice of a grid numerical method of integration. The Cartesian grid code limits the vertical resolution of a thin disc. Consequently the response of the disc to heating by the satellite is not correctly quantified. Furthermore, once the remnant satellite has merged with the disk, the position of it's centre of density becomes ill-defined by virtue of the satellite ceasing to exist as a bound entity; $\theta(t)$ will reflect this uncertainty for $t \gtrsim 2 - 3$ Gyr. With 32 mesh points spread over a length of $3R_d$, the position of the centre-of-density and the disc structure are resolved to $l \simeq 3R_d/32 \sim r_s/10$ when $r_s \approx R_d$. Hence the error on the angle θ may be estimated to be $\sin\theta \approx \theta = l/r_s \sim 1/10$ or $5°$ approximately. This puts into perspective the magnitude of the oscillations seen on Fig. 6 for $t \gtrsim 2 - 3$ Gyr, though without accounting for them fully. This leads us to conclude that the physical effect of the torque Γ by the disc on the satellite is qualitatively correct, although the quantities somewhat uncertain.

3.4 Orbital eccentricity

In Fig. 7 we plot the eccentricity evolution for satellites with mass $M_s = 0.1\,M_d$. The eccentricity is calculated by fitting straight lines to $r_a(t)$ and $r_p(t)$ (e.g. Fig. 7a) and interpolating $e(t)$ until the satellite has 10 % of its initial mass.

The orbital eccentricity does not remain constant as dynamical friction shrinks the orbit. The evolution of $e(t)$ depends on $e(t = 0)$ and $\theta(t = 0)$, but from Fig. 7b we observe that the general behaviour is for the orbits to become more radial with time. The only clearly evident exception is prograde model G2S100 ($e(0) = 0.7$), which shows a pronounced decrease of $e(t)$. In this case, dynamical friction from the flattened DMH plus disc is so large that the apo-galactic distance decreases much faster than the peri-galactic distance, as we can observe in Fig. 7a. Close inspection shows that this is merely the extreme of a general trend. Comparing the co-planar prograde orbits ($\theta = 0°$: GnS100, GnS100e, GnS100c; n= 1, 2) with the polar orbits ($\theta = 90°$: GnS190, GnS190e, GnS190c), it is evident that the former show a stronger sensitivity on initial eccentricity than the latter. The effect is such that circular co-planar prograde orbits gain eccentricity rapidly, whereas eccentric ($e(0) \approx 0.7$) prograde co-planar orbits circularize. Disc–satellite coupling
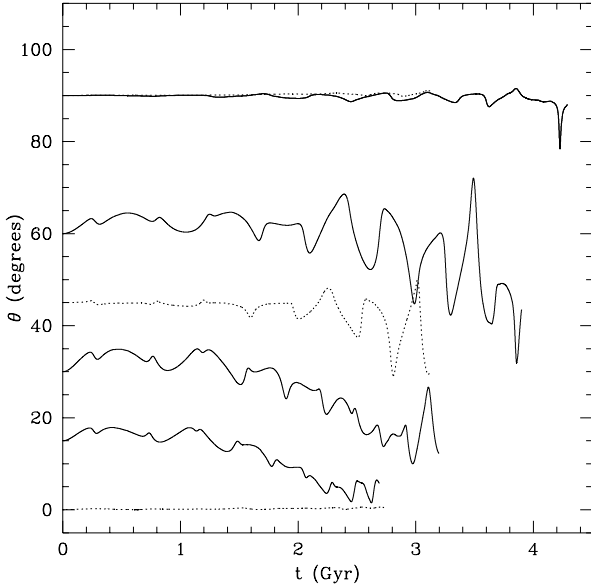
Figure 6. Evolution of the orbital inclination for models G2S100, G2S115, G2S130, G2S190 (full lines, satellites within the flattened DMH) and G1S145, G1S190 (dotted lines, satellites within the spherical DMH), until they retain 10% of their initial mass.

via dynamical friction and induction of spiral modes in the disc and associated transfer of angular momentum between satellite and disc are the likely reason, but we do not dwell longer on this, as disc-satellite coupling is not the main topic of this work, which in any case does not resolve the disc vertical structure. We merely state here that the data in Fig. 7b suggest that there is a stable eccentricity, $e_{stab} \approx 0.5$ for co-planar prograde orbits in our flattened DMH, such that $e(t)$ increases when $e(0) < e_{stab}$, whereas $e(t)$ slighty decreases when $e(0) > e_{stab}$, and $e(t) \approx e_{stab}$ for all t until satellite disruption, if $e(0) \approx e_{stab}$. However, if $e(0)$ is smaller than e_{stab}, $e(t)$ does not remain close to e_{stab} once it has reached this critical eccentricity. For our spherical DMH, $e_{stab} \approx 0.6$.

This behaviour agrees with that found by van den Bosch et al (1999). They perform numerical calculations using a galaxy models similar to G1, with satellite masses on the order of that of our models S1. They observe that the eccentricity remains remarkably constant for $e(0) \geq 0.6$. Unfortunately, they do not include calculations with lower initial eccentricity that we can compare with. We note in passing that Prugniel & Combes (1992) already found that initially circular orbits rapidly acquire eccentricity, as is also evident in the calculations of Fellhauer et al. (2000).

3.5   Orbital precession

The orbital plane of a satellite and its unbound particles precesses in a flattened potential which smears out the tidal debris stream. The precession angle, $P(t)$, is calculated by projecting the orbital angular momentum vector onto the galactic xy plane and measuring its change with time. In Fig. 8 we plot P for some of our models. The precession,
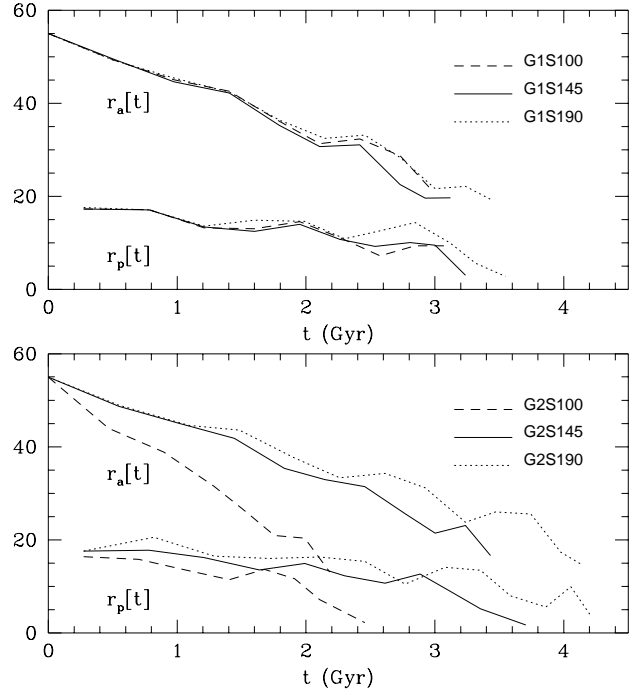

Figure 7. a: Evolution of the apo-galacticon and perigalacticon distance (in kpc) for the models with $e(t = 0) = 0.7$ until the satellite has 10 % of its initial mass.
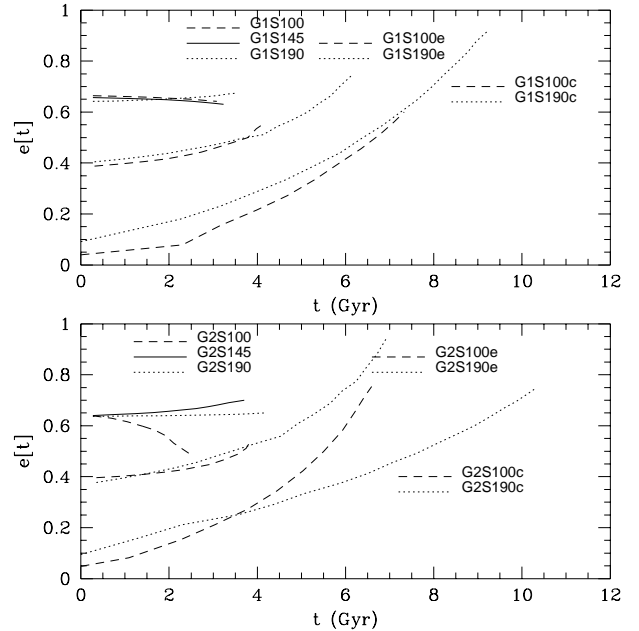

Figure 7 – *continued* **b:** The eccentricity evolution for the models shown in Fig. 7a. $e(t) = 1 - r_p(t)/r_a(t)$ and is measured by fitting the curves $r_a(t)$ and $r_p(t)$ by straight lines. We also plot it for the models with $e(0) = 0.45$ and $e(0) = 0$ (circular orbits), calculated following the same scheme.

dP/dt, increases at later times due to the anisotropy of the disc's potential, the satellite having decayed to its vicinity.

As expected, flattened DMHs lead to larger precession. Comparing models G1S145 (satellite within a spherical DMH) and G2S145 (satellite within a flattened DMH), we observe that the change of P is, respectively, $\simeq 50°$ and $\simeq 150°$, i.e, approximately three times larger at $t = 3$ Gyr.

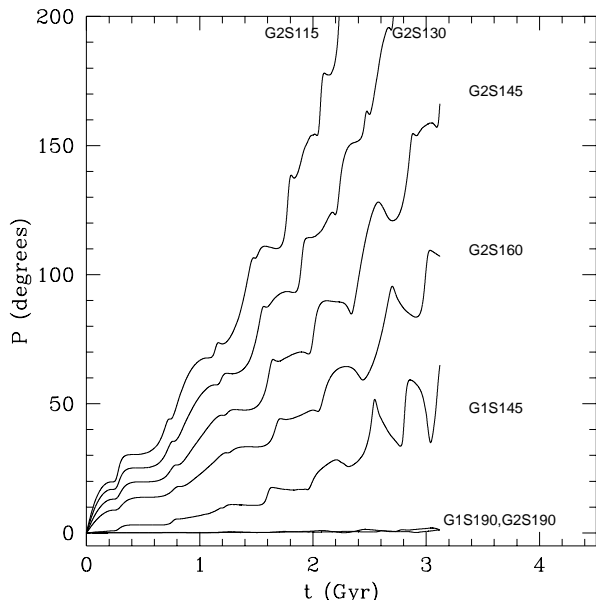**Figure 8.** The precession angle P for some of our models.

Figure 9. a: Deviation angles for all satellite particles from the initial orbital plane ($\theta = 45°$). The left column depicts model G1S145 (spherical DMH), and the right column shows G2S145 (flattened DMH). Rows show three time snaps (given in Gyr). In the last one, the satellite has been fully destroyed.

Since the DMH is spherical for models with G1 the precession of the orbital plane is due to the disc gravitational quadrupole moment. The orbital plane precesses faster the smaller its inclination is, orbits with $\theta \lesssim 45^o$ precessing by 180° in 3 Gyr. Polar orbits do not precess at all.

3.6 Tidal streams

The accretion history of the Milky Way and other major galaxies leaves signatures in the form of old tidal streams in the DMHs of these galaxies as found in observational surveys such as that of Dohm-Palmer et al (2001), or Martínez-Delgado et al (2001). The detection of the Sagittarius dwarf tails (Iabata et al 1994) therefore likely is a generic features of large galaxies.

Theoretical models of this process have shown good agreement with observations (Helmi & White 1999; Zhao et al. 1999; Helmi & de Zeeuw 2000). The changes in orbital inclination θ and the orbital precession in flattened systems imply that the tidal debris emanating from a disrupting satellite will significantly spread out in θ, which will make reconstruction of the accretion history of a major galaxy difficult if its DMH is flattened.

In Fig. 9 we plot the deviation angle of the satellite's particles from the initial orbital plane in three time snaps. This is done for models G1S145 and G2S145 (Fig. 9a, $\theta(0) = 45°$), and for G1S190 and G2S190 (Fig. 9b, $\theta(0) = 90°$). The first time-snap shows satellite particles after first passage through perigalacticon at $t = 0.62$ Gyr, the second one is at an intermediate time ($t = 1.52$ Gyr) while the last frame is at a late stage of the satellite orbit. The debris does not remain in the initial orbital plane. This effect becomes more pronounced the closer the satellite is to the galaxy's centre, when the mass loss (Fig. 4) and the oscillations of orbital inclination (Fig. 6) primarily occur, and the larger
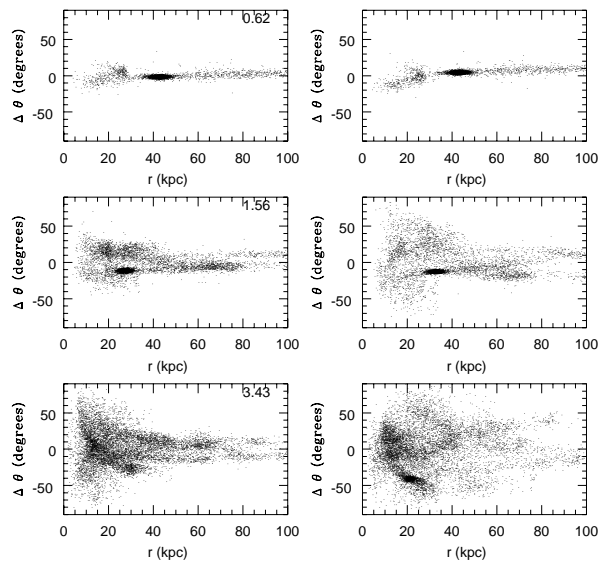
the number of perigalacticon passages is. From Fig. 9**a** we also observe that the deviations from the orbital plane are enhanced when the DMH is flattened since satellite orbits within oblate DMHs align with the symmetry plane (i.e. $\theta(t) \rightarrow 0$). Fig. 9**b** shows that the spread of satellite debris is much smaller for satellites in polar orbits than for those with intermediate inclinations, since inclination decay and oscillations vanish for polar orbits.

4 CONCLUSIONS

In order to assess the importance of dynamical friction in extended oblate DMHs on the distribution of satellite galaxies around their primary, we perform self-consistent N-body computations of satellite galaxies with masses amounting from 10 to 20 per cent of the primary's disc. The satellites are placed on different orbits in spherical and flattened DMHs that have embedded galactic discs and bulges.

The calculations with spherical DMHs lead to results in good agreement with those obtained by Velazquez & White (1999). Modest differences in quantities are attributed to the increased mass resolution of our calculations compared with theirs, as well as different linear resolution (grid size versus smoothing length of their TREE algorithm).

Satellites evolving in spherical DMHs on prograde orbits relatively to the primary galaxy's disc rotation decay faster than satellites on retrograde orbits or on polar orbits. This results from orbital resonances between the disc and the satellites.

Of particular interest, however, is that our results demonstrate that non-isotropic dynamical friction in flattened DMHs works as a removal mechanism of satellites with low-inclination orbits, whereas it enhances the survival time
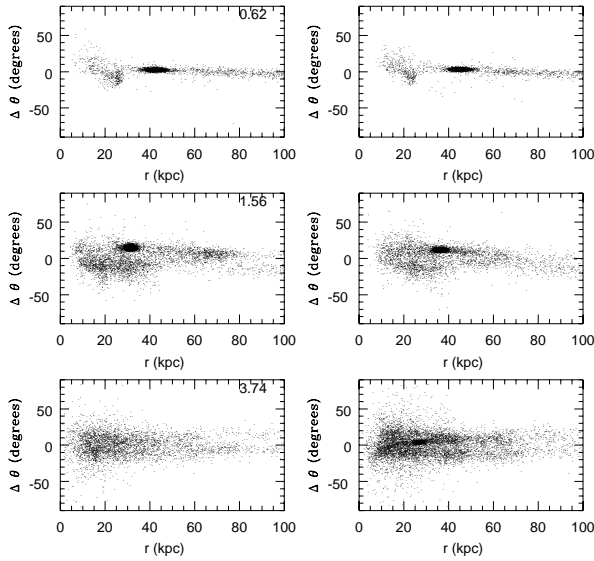
Figure 9 – *continued* **b:** As Fig. 9a but for models G1S190 (spherical DMH) and G2S190 (flattened DMH), with initial inclination $\theta = 90°$.

of satellites on near polar orbits. Thus, satellites on polar orbits survive about 70 per cent longer than satellites on orbits that have a small inclination relative to the primary galaxy's disc (Table 4), irrespective of the relative orbital sense (Fig. 5) in an oblate DMH with axis ratio $q_h = 0.6$. This is the key result of this investigation.

This result helps understand the distribution of dwarfs galaxies in the Milky Way. Since they are mainly distributed near the galactic pole (Carney et al. 1987) we may infer a selection of survivor dwarfs from a primordial population. The accelerated orbital decay and alignment with the disc of dwarfs within a flattened halo would go some way towards accounting for the data. However if the masses deduced for these satellites (10^8 solar, compared with 10^9 for our models) is a good measure of their mass at the formation time, our computations indicate times as long as a Hubble time for effective mergers. Discrepancies in timescale may well be accounted for if we substitute for the isothermal halo the more concentrated NFW (Navarro, Frenk & White 1995) models or haloes with a steeper cusp (Moore et al. 1998): when each halo model is scaled to the same integrated mass inside the solar radius, the particle velocity dispersion in these models drops faster with radius than for isothermal spheres. Because of the strong dependence of friction on velocity dispersion, this would reduce the timescale for orbital decay very much and offset the effect of reduced satellite masses. We have not, however, performed calculations with different halo mass profiles.

Our computations further show that satellites on orbits with eccentricity $e \gtrsim 0.5$ and with masses larger than 10 per cent of their primary galaxy's disc merge within only a few Gyr with the primary galaxy. The time it takes to merge increases with decreasing orbital eccentricity (Fig. 5). We therefore deduce that massive satellites around distant galaxies, such as typically enter the samples that show the

Holmberg effect, may be preferentially on near-circular polar orbits or on orbits with apo-galactica further away from their primary galaxy than about 130 kpc.

The calculations also suggest that there exists a critical eccentricity, e_{stab}, for co-planar prograde orbits such that initial eccentricities that are close to e_{stab} remain within the vicinity of this 'stable' value, whereas initial orbital eccentricities that differ from e_{stab} evolve towards the critical value but the orbit keeps evolving past e_{stab} (Section 3.4). For our oblate DMH, $e_{\mathrm{stab}} \approx 0.5$, whereas for the spherical DMH $e_{\mathrm{stab}} \approx 0.6$.

We also note that the high precession rates of satellite orbits in flattened DMHs and the decrease in orbital inclination leads to tidal debris streams being completely smeared apart for initially inclined orbits.

We want to comment that, despite our use of only two values for the satellite mass in our calculations, this range seems to be representative to reproduce the typical mass of the satellite that Holmberg (1969) and Zaritsky & González (1999) find in their observations when the initial apo-galactic distances is selected properly (Ibata et.al 2001). As Tormen (1997) finds in his numerical calculations of hierarchical galaxy clusters history, more massive satellites ($\sim 10^{11}$) are unlikely to survive due to the large drag force they suffer. On the other hand, though less massive satellites ($\sim 10^8$ solar) feel a negligible drag force, they are quickly disrupted after some peri-galacticon passages due to their low binding energy.

This paper has sought to quantify the effect of aspherical DMHs on the orbits of galactic satellites. The analysis suggests enhanced Holmberg decay, yet what can we say of a population of satellites as a whole? Our model satellites require a few orbits around the host galaxy if dynamical friction is to be effective. Thus within one Hubble time a satellite would require = 5 revolutions (say) or $t = 2$ Gyr for a single revolution at most. In the Milky Way the orbital time $t = 200$ Myr at $r = 10$kpc; assuming an isothermal halo with $\rho \propto r^{-2}$, the critical orbital time $t = 2$ Gyr would be found at $r = 50$ kpc or so. In other words, satellites that are too far from the host galaxy will not have time to experience dynamical friction and hence will not have suffered Holmberg decay. On the other hand, satellites closer to their host galaxy will merge quickly through the process described here. Zaritsky et al. (1999) have noted that satellite populations tend to remain isotropically distributed for satellites with $r > 50$ Kpc.

A more elaborate study is under way, and ultimately we aim at making a statistical study of a modelled observational sample to infer if the Holmberg effect can indeed be produced by flattened DMHs.

REFERENCES

Bahcall J.N., Schmidt M., Soneira R.M., 1982, ApJ, 258, L23

Binggeli B., Sandage A., Tarenghi M., 1984, AJ, 89, 64

Binney J., 1977, MNRAS, 181, 735

Binney J., Tremaine S., 1987, Galactic Dynamics. Princeton University Press, Princeton, New Jersey

Binney J., 1992, ARA&A, 30, 51

Boily C.M., Peñarrubia J., Kroupa P., 2001, NewA, 6, 27 (BKP)

Carney B., Lathman D.W., 1987, in Kormendy J., Knapp G.R., eds, Proc. IAU Symp 117, Dark matter in the Universe. Reidel, Dordrecht, p.39

Chandrasekhar S., 1960, Principles of Stellar Dynamics. Dover, New York

Colpi M., Mayer l., Governato f., ApJ, 525, 720

Dohm-Palmer R. C., Helmi A., Morrison H., Mateo M., Olszewski E. W., Harding P., Freeman K. C., Norris J., Shectman S. A., ApJ, 555, 37

Dubinsky J., 1994, ApJ, 431, 617

Fellhauer M., Kroupa P., Baumgardt H., Bien R., Boily C. M., Spurzem R., Wassmer N., 2000, NewA, 5, 305

González A.H., Williams K.A., Bullock J.S., Kolatt T.S., Primack J.R., 1999, ApJ, 528, 145

Helmi A., White S.D.M., 1999, MNRAS, 307, 495

Helmi A., de Zeeuw P.T., 2000, MNRAS, 319, 657

Hernquist L., 1990, ApJ, 356, 359

Hernquist L., 1993, ApJS, 86, 389

Holmberg E., 1969, Arkiv. Astr, 5, 305

Ibata, R. A., Gilmore, G. & Irwin, M. J. 1994, Nature 370, 194

Ibata R., Lewis G.F., Irwin M., Totten E., Quinn T., 2001, ApJ, in press

Johnston K., Sigurdsson S., Hernquist L., 1999, MNRAS, 302, 771

Keeton C.R., Kochanek C.S., 1998, ApJ, 495, 157

King I.R., 1966, AJ, 71, 65

Klessen R.S., Kroupa P., 1998, ApJ, 498, 143

Kroupa P., 1997, NewA, 2, 139

Lewis J.R., Freeman K.C., 1989, AJ, 97, 139

Maller A.H., Flores R.A., Primack J.R., 1997, ApJ, 486, 681

Maller A.H., Simard L., Guhathakurta P., Hjorth J., Jaunsen A.O., Flores R., Primack J.R., 2000, ApJ, 533, 194

Martínez-Delgado D., Aparicio, A., Gómez-Flechoso, M. A., Carrera R., 2001, ApJ, 547, 133

Moore, B., Quinn, T., Governato, F., Stadel, J. & Lake, G. 1999, MNRAS 310, 1147

Navarro, J.F., Frenk, C.S. & White, S. D. M. 1997, ApJ 490, 493

Olling R.P., Merrifield M.R., 2000, MNRAS, 311, 361

Persic M., Salucci P., Stel F., 1996, MNRAS, 281, 27

Pfenniger D., Combes F., Martinet L., 1994, A&A, 285, 79

Piatek S., Pryor C., 1995, AJ, 109, 1071

Prugniel Ph., Combes F., 1992, A&A, 259, 25

Quinn P.J., Goodman J., 1986, ApJ, 306, 472

Sciama D., 1990, MNRAS, 244, 1

Spitzer L., 1942, ApJ, 95, 329

Stenmetz M., White D.M., 1997, 288, 545

Taylor J.E., Babul A., 2000, astro-ph/0012305

Tormen G., 1997, MNRAS, 290, 411

de Vaucouleurs G., 1948, Annales d'Astrophysique, 11, 247

van den Bosch F., Lewis, G.F., Lake G., Stadel J., 1999, ApJ, 515, 50

Velázquez H., White S.D.M., 1999, MNRAS, 304, 254 (VW)

Weinberg M.D., 2000, ApJ, 532, 922

Whade M., Donner K.J., 1996, A&A, 312, 431

Zaritsky D., White S.D.M., 1994, ApJ, 435, 599

Zaritsky D., González A., PASP, 111, 1508

Zhao H., Johnston K.V., Hernquist L., Spergel D.N., 1999, A&A, 348, L49